

Transition in a numerical model of contact line dynamics and forced dewetting

S. Afkhami^{1a}, J. Buongiorno^b, A. Guion^b, S. Popinet^c, R. Scardovelli^d,
S. Zaleski^c

^a*Department of Mathematical Sciences, New Jersey Institute of Technology, Newark, NJ, USA*

^b*Nuclear Science and Engineering Department, Massachusetts Institute of Technology, Cambridge, MA, USA*

^c*Sorbonne Universités, UPMC Univ Paris 06, CNRS, UMR 7190, Institut Jean le Rond d'Alembert, F-75005, Paris, France*

^d*DIN – Laboratorio di Montecuccolino, Università di Bologna, 40136 Bologna, Italy*

Abstract

We investigate the transition to a Landau–Levich–Derjaguin film in forced dewetting using a quadtree adaptive solution to the Navier–Stokes equations with surface tension. A discretization of the capillary forces near the receding contact line is used that yields an equilibrium for a specified contact angle θ_Δ called the numerical contact angle. Despite the well-known contact line singularity, dynamic simulations can proceed without any explicit additional numerical procedure, yielding an implicitly dynamic contact angle model. We investigate angles from 15° to 110° and capillary numbers from 0.001 to 0.1. The observed dynamics at small capillary number are in agreement with the Cox–Voinov theory, and yield a dynamic contact angle measurable at scales larger than the grid size Δ that depends logarithmically on the distance to the contact line. The fit to the logarithmic dependence involves a “microscopic” distance r_m that characterizes the numerics. This distance r_m is proportional to Δ/ϕ , where ϕ is a scaling factor or gauge function. This scaling factor is shown to depend only on the equilibrium angle θ_Δ and the viscosity ratio. We rework the prediction of Eggers [Phys. Rev. Lett., vol. 93, pp 094502, 2004] of the critical capillary number for the Landau–Levich–Derjaguin forced dewetting transition to include finite angles θ_Δ and the gauge function ϕ . The numerical results are in agreement with this theory. An analogy can be drawn between the numerical contact angle condition and a regularization of the Navier–Stokes equation by a partial Navier slip model. The analogy leads, at small angles, to a value for the numerical length scale proportional to the slip length. Thus the microscopic length found in the simulations is a kind of numerical slip length. The knowledge of this microscopic length scale and the associated gauge function can be used to realize grid-independent simulations of general fluid-mechanical

¹Corresponding author email address: shahriar.afkhami@njit.edu

problems involving dynamic contact lines. This procedure for grid-independent simulations improves upon the one suggested previously by two of the authors, as it allows the use of general angles and viscosity ratios.

Keywords: Dynamic contact line, Contact angle, Contact line stress singularity, Slip boundary condition, Landau–Levich–Derjaguin film, Forced dewetting, Wetting failure, Cox-Voinov model, Volume-of-Fluid (VOF), Gerris, Slip length, Navier slip, Partial slip.

1. Introduction

Wetting of solids by liquids, in which a liquid displaces another fluid on a solid substrate, is an ubiquitous phenomenon with applications ranging from coating [1] and tear films on the cornea [2] to micro-layer formation in wall boiling [3, 4] and CO₂ sequestration [5]. However, despite the abundance of applications, the precise mechanism of wetting is only partially understood. From the numerical modeling point of view, difficulties arise due to the highly multiscale nature of the problem (length scales extending from the macroscopic to the molecular sizes). Another major challenge in numerical simulations is the so-called contact line singularity that arises when a continuum description of moving contact lines is used in combination with a no-slip boundary condition at the liquid-solid interface. Because of this singularity, the continuum description is untenable below a certain scale. Thus a transition to a different, nonsingular physics must occur as the scale is reduced. The most obvious such transition is the appearance of molecular effects at nanometer scales. However a variety of other “microscopic” contact line physics, some of which would “kick-in” at scales much larger than the nanometer, have been considered in the literature. It is difficult to be exhaustive but these involve precursor film models [6], diffuse-interface models [7, 8, 9, 10] and the related issue of evaporation [11], interface formation models [12, 13], and surface roughness [14]. The reader may find references to other mechanisms in review papers [15, 16, 17, 18]. Slip of the contact line is of particular interest as a possible physical mechanism to allow motion of the contact line on the microcopic scale, mostly because it conveniently does not require to change the Navier–Stokes equations, see e.g. [19, 20, 21, 22, 23, 24, 25, 26, 27]. However, numerical simulations involving slip-length modeling are unfeasible in most physical problems since the true slip should be related to molecular interactions between the liquid and the solid substrate [15], which based on experimental measurements lies in the nanometer range [28, 29]. Thus a regularization of the numerics based on the slip length leads to computationally inconvenient large ratios of scales. On the other hand, if no regularization is performed or if the slip length is dependent on grid spacing, the moving contact line solutions become themselves dependent on grid spacing (see e.g. [26, 30, 31]).

The main motivation of this paper is to make progress towards accurate and reliable simulations of flows containing contact line dynamics, specifying the

interface angle at an intermediate range, which in turn serves as a boundary condition for the macroscopic dynamics. A practical approach can therefore be a hybrid model in which only the macroscopic scale is numerically resolved and the microscopic description of contact line region is included through a hydrodynamic theory [26, 32, 33] or other microscopic mechanisms [6, 34].

In this paper we do not attempt to implement a sophisticated hybrid model, but instead take an existing, simple numerical method already used for static cases and apply it “as it is” for dynamic simulations. This is a kind of “implicit modeling” approach similar to the implicit subgrid scale modeling frequent in Large Eddy Simulations of turbulence. This approach has the merit of simplicity, and it then remains to assess how this “numerical boundary condition” affects the flow.

We study a specific, complex physical problem: the dewetting transition. In a number of applications, the interface is forced to move along a solid in a manner that can result either in a receding contact line or on the formation of a thin film on the solid. One example of such a flow is the withdrawing-tape experiment whose geometry is illustrated on Fig. 1. A solid substrate is withdrawn on the left from a viscous liquid pool of mostly quiescent liquid. The interface may either sustain a stationary state meniscus, if below a critical capillary number, Ca_{cr} , or to continue to move up the substrate until depositing a thin film to arbitrary heights. The latter is called a Landau–Levich–Derjaguin (LLD) film [35, 36]. This transition can be understood in terms of the imbalance between the surface tension, gravity and viscous forces that leads to the vanishing of the contact line. The analysis of the transition process on a partially wetting substrate is however complicated due to the singularity of the moving contact line. On one hand, Eggers and his coworkers, in a series of papers [37, 38, 39] provided a hydrodynamic prediction, based on the lubrication approximation theory, of the critical capillary number Ca_{cr} . Cox [22] and Voinov [40] described, on the other hand, how the singularity drove a peculiar curved form of the fluid wedge at small Ca . We use an analog of these theories in the case where the real microscopic physics are replaced by the grid-scale numerics, to predict the microscopic length. This microscopic length in turn allows to predict the numerically observed transition. We shall show that 1) the microscopic length is entirely described by a gauge function depending only on the equilibrium contact angle imposed numerically and 2) that the knowledge of this numerical gauge function can be used to mimic the effect of actual subgrid scale microscopic physics, so that the simulations become grid independent. This second point offers an extension of the theory in [26].

The rest of this paper is organized as follows. In Sec. 2, we describe the physical problem and explain our choice of parameters. In Sec. 3, we describe the computational setup and the numerical method for the implementation of the contact angle. In Sec. 4, we report the results of our simulations including the method for determining the critical capillary number Ca_{cr} . In Appendix A, we give a theoretical analysis of these results and introduce the main new theoretical concept of this paper, the gauge function ϕ . We compare our results to hydrodynamic theories obtained in the case of Navier slip in Sec. 6. In Sec. 7,

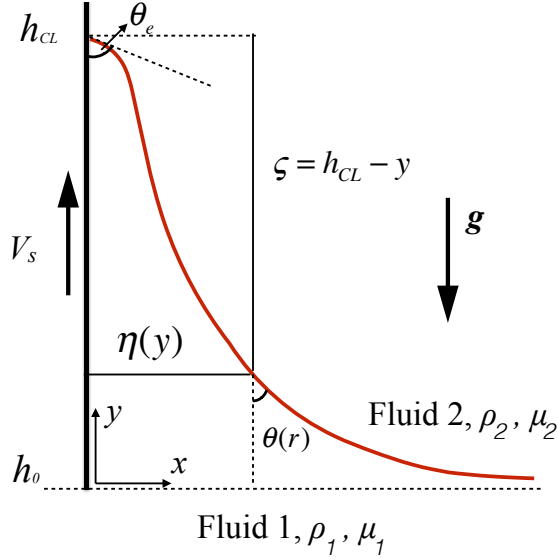


Figure 1: Schematic illustrating the contact angles θ_e and $\theta(r)$, corresponding to length scales λ and r , respectively. h_{CL} represents the contact line height and h_0 is the unperturbed initial interface profile. $\zeta = h_{CL} - y$ is the vertical distance of the interface at y from the contact line. $\eta(y)$ is the horizontal distance of the interface from the solid substrate.

we discuss the connection with theories where the microscopic angle varies with the capillary number as in the Molecular Kinetic Theory. In Sec. 8 we apply the concepts developed above to describe an improved procedure for obtaining grid-independent computations of problems with dynamic contact lines. Finally, we draw our conclusions in Sec. 9.

2. Problem setup: forced dewetting

We consider a solid plate being withdrawn from a liquid reservoir with a constant velocity $V_s > 0$. The computational domain is $0 \leq x, y \leq L$, with fluid 1 occupying $y < h_0$ and fluid 2 occupying $y > h_0$ at $t = 0$ (see Fig. 1). The viscosity and density of fluid $i = 1, 2$ are μ_i and ρ_i , respectively. The capillary number is defined as

$$\text{Ca} = \mu_1 V_s / \sigma,$$

where μ_i is the viscosity of fluid i and σ the surface tension. We set $L \approx 9 l_c$, where l_c is the capillary length $l_c = \sqrt{\sigma / [(\rho_1 - \rho_2)g]}$ with g the gravitational acceleration. The Reynolds number is then defined based on the capillary length as $\text{Re} = \rho_1 V_s l_c / \mu_1$. Thus $\text{Re} = \text{Ca} \text{Mo}^{-1/2}$ where the Morton number is

$$\text{Mo} = \frac{(\rho_1 - \rho_2) g \mu_1^4}{\rho_1^2 \sigma^3}. \quad (1)$$

Setup	$N_G = \rho_1^2 V_s^3 / (\mu_1 (\rho_1 - \rho_2) g)$	$\text{Re} = \rho_1 V_s l_c / \mu_1$	$1/q = \mu_1 / \mu_2$	ρ_1 / ρ_2
A	25/64	-	1	5
B	-	1	1	5
C	-	1	50	5

Table 1: Summary of the simulation Setups. When no value is indicated, the corresponding number is computed from the other numbers using Eq. (3).

We define a “gravity wave damping number” as

$$N_G = \frac{\rho_1^2 V_s^3}{\mu_1 (\rho_1 - \rho_2) g}. \quad (2)$$

Indeed, the wavelength of gravity waves traveling at the same speed as the withdrawing tape is $L_{gw} = \rho_1 V_s^2 / [(\rho_1 - \rho_2)g]$ and it can be connected to N_G through $N_G = \rho_1 L_{gw} V_s / \mu_1$. Thus N_G is also the Reynolds number based on the wavelength of gravity waves. It is related to the capillary length Reynolds number by

$$\text{Re} = N_G^{1/2} \text{Ca}^{-1/2}. \quad (3)$$

We use several setups for the simulations, presented in Tab. 1. In Setups A and B, for relatively more efficient computations, we set the ratios of physical properties to moderate values with the viscosity ratio $\mu_1/\mu_2 = 1$ and the density ratio $\rho_1/\rho_2 = 5$. The other parameters are chosen in the following way. In Setup A, the number N_G is arbitrarily set to $N_G = 25/64$. (It is the value corresponding to the arbitrary choices of $\rho_1 = 5, \rho_2 = 1, g = 16, \mu_1 = 1, V_s = 1$.) Thus from Eq. (3) the Reynolds number based on l_c varies as

$$\text{Re} = \frac{5}{8} \text{Ca}^{-1/2}. \quad (4)$$

As a result the Reynolds number based on l_c increases as the capillary number decreases. Varying the Reynolds number between 0 (Stokes approximation) and $\text{Re} = 3$ has no effect on the results, however increasing Re beyond this value introduces significant inertial effects and interface oscillations that modify the conclusions of our investigations. At small Ca , we therefore switch to Setup B, where N_G is free to vary and the Reynolds number based on l_c is fixed to $\text{Re} = 1$. In a final set of simulations (Setup C), we keep $\rho_1/\rho_2 = 5$ and $\text{Re} = 1$ but let $\mu_1/\mu_2 = 50$. This allows to bring the simulations closer to air/water conditions without encountering the numerical problems arising with very large density ratios.

We begin the simulations by considering a flat interface between the two fluids initially at the height $h_0 \approx 3.1 l_c$. A no-slip boundary condition is prescribed at the substrate ($x = 0$). Symmetry boundary conditions are imposed on the right ($x = L$), top ($y = L$), and bottom ($y = 0$) boundaries of the domain. We note that we have checked that the results are insensitive to the computational domain size.

In the neighborhood of the contact line, no specific choice of parameters is required except the equilibrium or static contact angle that is specified in the numerical model. It is also expected that the numerical model leads to a solution varying continuously with the withdrawing tape velocity, so that the contact angle tends to the static contact angle as Ca tends to zero. How simulations with a contact angle are performed is described in the next section.

3. Numerical model

We use Gerris [41, 42, 43] to numerically solve the Navier–Stokes, continuity and density equations,

$$\rho(\partial_t \mathbf{u} + \mathbf{u} \cdot \nabla \mathbf{u}) = -\nabla p + \nabla \cdot [\mu(\nabla \mathbf{u} + \nabla \mathbf{u}^\top)] + \sigma \kappa \delta_s \mathbf{n} + \rho \mathbf{g}, \quad (5)$$

$$\nabla \cdot \mathbf{u} = 0, \quad (6)$$

$$\partial_t \rho + \mathbf{u} \cdot \nabla \rho = 0, \quad (7)$$

respectively. Here, \mathbf{u} is the velocity field, p the pressure, $\rho = \rho_1 \chi + \rho_2(1 - \chi)$, $\mu = \mu_1 \chi + \mu_2(1 - \chi)$, κ is the interface curvature, \mathbf{n} the normal to the interface (pointing from fluid 1 to fluid 2), δ_s the delta function centered at the interface, $\rho \mathbf{g} = -\rho g \hat{y}$ the body force due to gravity and \hat{y} the unit vector in the y -direction, and χ ($= 1$ in fluid 1 and 0 in fluid 2) the characteristic function, where we use the approximation $\delta_s \mathbf{n} = \nabla \chi$. Note that Eq. (7) is equivalent to

$$\partial_t \chi + \mathbf{u} \cdot \nabla \chi = 0, \quad (8)$$

which is solved using the Volume-of-Fluid (VOF) interface capturing method [43, 44, 45]. The Continuous Surface Force (CSF) method is used for the surface tension force with curvature computed using the Height-Function method [43]. Viscous forces are implemented using a partially implicit method described in [46].

It is useful to discuss in more detail the procedure used near the contact line. First, without giving the full details that can be found in the references, let us outline the procedure used away from the contact line. There, the VOF discretization of Eq. (8) consists in the definition of a variable $C_{i,j}$ on each grid point i, j that is equal to the volume fraction of the reference fluid, fluid “1”, in the cell. The VOF method proceeds in two steps, first the reconstruction of the interface followed by its advection. In the first part of the reconstruction step, the interface normal $\mathbf{n} = (n_x, n_y)$ in cell i, j is determined from the values $C_{i,j}$ in neighboring cells using the “mixed Youngs-centered” (MYC) method (see [47]). In the second part of the reconstruction step, the position of a linear segment representing the interface in the cell is determined using elementary geometry (see [47]) from the knowledge of \mathbf{n} and $C_{i,j}$. Thus the equation of the segment is written

$$n_x x + n_y y = \alpha, \quad (9)$$

where the scalar α characterizes the position of the interface. The knowledge of \mathbf{n} and α is then used in turn in the second, advection step, where the interface

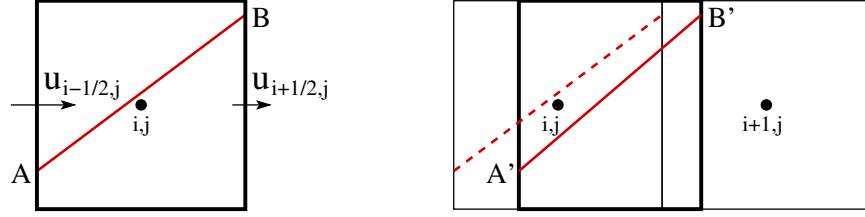


Figure 2: Advection of the interface along the x -direction: standard “Lagrangian Explicit” or “CIAM” method with the cell centered at grid point i, j being advected and expanded/compressed by the flow, in this case it is compressed since $\partial u / \partial x < 0$; before advection (left) and after advection (right).

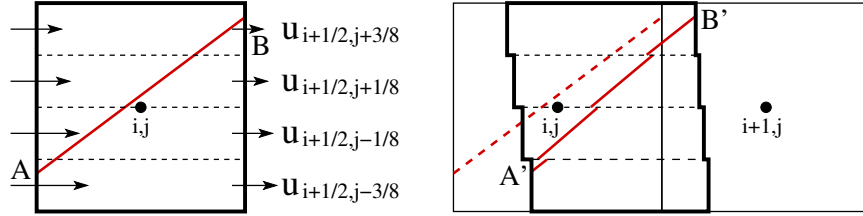


Figure 3: Advection of the interface along the x -direction with the cell subdivided in $m = 4$ equal bands: with “banding” the effect of shearing, that is a $\partial u / \partial y$ derivative, is taken into account more accurately than in the standard method; before advection (left) and after advection (right).

is displaced by the fluid velocity field. On Fig. 2, the standard “Lagrangian-Explicit” (see [47]) advection step is represented. It is useful to describe the advection process in some detail. The collocated velocities $u_{i,j}, v_{i,j}$, defined on cell centers, are used to compute an auxiliary set of velocities $u_{i+1/2,j}$ and $v_{i,j+1/2}$ on different cell face centers using a projection method. The determination of the motion of the piece of interface shown on Fig. 2 is identical to the “Lagrangian Explicit” or “CIAM” method [43, 47]. However a recent implementation in Gerris uses a “banded” advection. In this approach, the cell is subdivided in m equal bands, the default being $m = 4$ as on Fig. 3, and the advection is performed separately in each band. After that, the bands in the cells are aggregated to produce the final volume fraction. This ensures a better representation of shearing or rotating velocity fields, while volume conservation is enforced by the requirement that the average of the horizontal velocity in the bands, for example, on the right side of the cell in Fig. 3 (left panel) to be equal to the face center velocity $u_{i+1/2,j}$.

We next present a test case to clearly illustrate the improvement when using the “banded” advection [48]. In this test case, a straight interface is advected by a pure shear flow, at a shear rate of 1, in a 1×1 computational domain. The exact solution is simply a rotation of the interface around the center of the domain. We note that both the interface and the velocity field are described

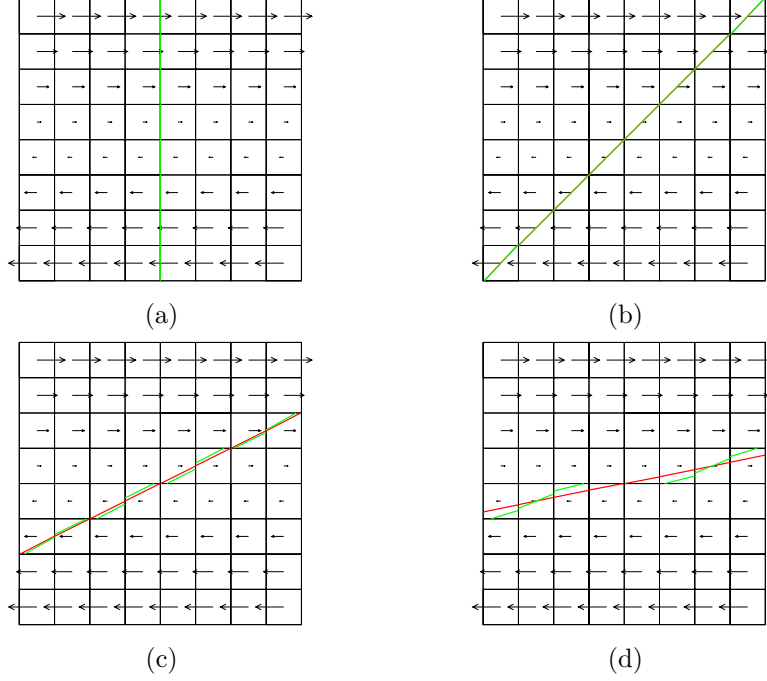


Figure 4: Evolution of the VOF interface in a shear flow at a shear rate of 1. (a) $t = 0$, (b) $t = 1$, (c) $t = 2$, and (d) $t = 5$; for $m = 1$ (—) and $m = 4$ (—).

exactly by a second-order method. Fig. 4 illustrates the rotation of the straight interface under the shear flow. The green segments are the VOF reconstructed interfaces obtained with $m = 1$ and the red segments are when using a “banded” advection method with $m = 4$ bands. Fig. 5 illustrates the evolution of the error with time. For $t = 1$, the interface is at 45 degrees and the errors in fluxes cancel out exactly.

In order to compute capillary forces, we use the Height-Function method, in which the local height of the interface is computed from summing over a column of cells with

$$h_i = \sum_{j=j_1}^{j_2} C_{i,j} \quad (10)$$

where j_1 is the index of the bottom cell in the column and j_2 the index of the top cell. When the bottom cell is full ($C_{i,j_1} = 1$) and the top cell is empty ($C_{i,j_2} = 0$), and there is a single interface in the column, the height h_i approaches the exact interface height to second order [49]. Using finite differences of the local Height-Function then provides the curvature, which is used to compute the surface tension force by the CSF method (see [43]).

Near the contact line, we consider a cell i, j containing the contact line C

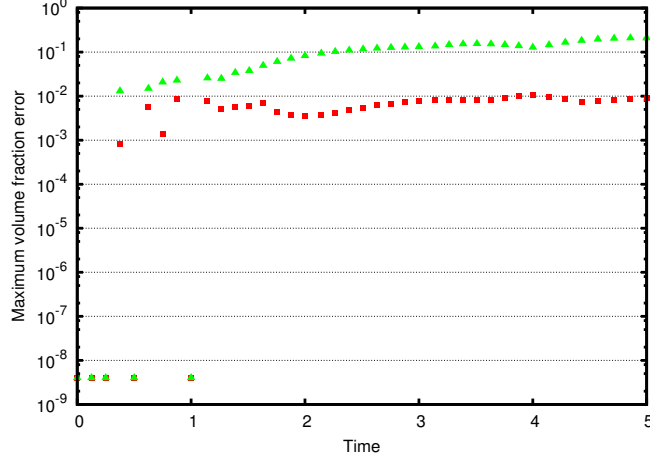


Figure 5: Volume fraction error as a function of time; for $m = 1$ (\blacktriangle) and $m = 4$ (\blacksquare).

as shown on Fig. 6(a). The solid-fluid boundary is located exactly on the lower boundary of this cell. (Other locations for the solid boundary have not been explored by the authors.) In that case, the MYC method is not used and in fact cannot be used because of insufficient data in the neighboring cells. Instead, the normal vector is recovered trivially from the specified contact angle θ_Δ as $n_x = -\sin(\theta_\Delta)$, $n_y = \cos(\theta_\Delta)$. The value of α in Eq. (9) is then obtained using elementary geometry. The interface can then be linearly extended into the solid cell $i, j - 1$ as shown by the dashed line on Fig. 6(b). It is assumed there is no other contact line in the immediate neighborhood. The computation of the normal in cell $i + 1, j$ is not immediately possible using the MYC method, but this difficulty is easily circumvented by assigning “ghost” $C_{i,j}$ values to the cells in the first solid layer $j - 1$.

Then as shown on Fig. 6(c), the heights h_i and h_{i+1} can be reconstructed in columns i and $i + 1$. To construct the height h_{i-1} in the column beyond the contact line a first order extrapolation of the form $h_{i-1} = h_i - \tan(\theta_\Delta)\Delta$ is used, where Δ is the local grid size.

The heights over the three columns $i - 1, i, i + 1$ can be used to compute the curvature in the cell containing the contact line C. This is a good approximation when both the interface slope and its curvature are small enough. Alternatively, it is possible to fit a parabolic approximation of the interface through the two heights h_i and h_{i+1} and the contact point C of Fig. 6(a) computed from Eq. (9).

For vertical interfaces one uses “widths” w_j instead, as shown on Fig. 6(d). Finally when neither heights nor widths are available, several other strategies are used to compute the curvature, as outlined by Popinet [43], using either a mixture of heights and widths (the so-called mixed-heights method) or if the mixed-heights method fails, a polynomial fit to the mid points of the segments

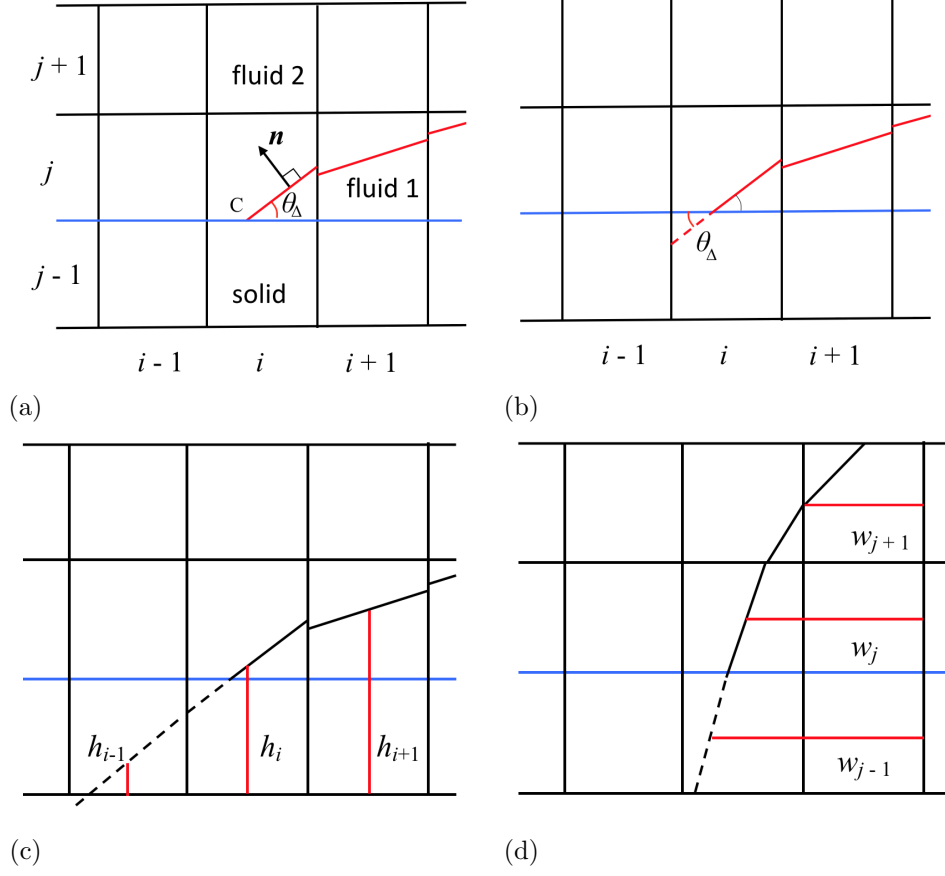


Figure 6: Reconstruction of the interface and height functions in the vicinity of the contact line. (a) Reconstruction in cell i, j . (b) Linear extension to cell $i, j - 1$. (c) Standard Height-Function method in columns i and $i + 1$ together with extrapolation of the height to cell $i - 1$. (d) Same as (c) but with widths in horizontal segments $j - 1, j$ and $j + 1$.

in each cell. These alternative strategies can be adapted to the vicinity of the contact line, provided extrapolations of the volume fraction $C_{i,j}$ and slope in cells $i-1, j-1$ and $i, j-1$ are used. It is important to remark that the Height-Function method for curvature (without mixed heights) always provides a curvature for $\kappa\Delta$ small enough. The critical value of $\kappa\Delta$ was estimated independently by one of the authors through tests on a large number of random circles showing that the minimum value of $\kappa\Delta$ at which the Height-Function always works is about 0.06.

Once the interface positions and the curvature are computed, there is no special difficulty in computing the velocity field using the standard methods. No special provision is made for the discontinuity of velocities or the divergence of viscous stresses and pressures, which are computed as elsewhere in the domain using finite volumes and finite differences.

We note however that the Gerris code uses the staggered (face) velocities to advect interface pieces, and therefore, in the contact line cell C on Fig. 6, the tangential (face) velocities used for advecting the interface in that cell will not be equal to the solid velocity, since they are defined half-a-cell above the solid boundary which is at $j-1/2$ on Fig. 6. Intuitively, this allows a kind of effective slip. However the amount of slip is reduced by the banding method described above and shown in Fig. 3.

It is interesting to note that at the scale Δ of the cell i, j the interface and the velocity field are represented in a coarsely averaged manner that is very far from capturing the flow reversal expected inside the fluid 1 wedge (although on scales larger than Δ this flow is well captured). Whether it is possible or desirable to have a more sophisticated discretization approach near the contact line is beyond the scope of this paper.

The Gerris code uses quadtree grids (or octree in 3D), that allow to refine the grid where necessary. This is a very useful feature for dynamical contact line problems as it allows to use a very small grid size Δ in the immediate neighborhood of the contact line and a larger grid size elsewhere.

4. Results: transition to film formation in forced dewetting

We focus on the problem of a partially wetting substrate withdrawn from a liquid reservoir. We find two parameter ranges: first, the stationary regime, for which the contact line motion along the substrate can evolve to a steady state, as $\tau \rightarrow \infty$, where the nondimensional time $\tau = V_s t / l_c$; second, the unsteady regime for which a steady state solution cannot be found and the contact line height continues to increase, covering the substrate by a film. All the results presented in this section are for Setup A, unless stated otherwise. We begin by presenting various scenarios characterized by different nondimensional grid sizes, Δ/l_c , and the imposed contact angle, θ_Δ . Fig. 7 shows the instantaneous contact line height, h_{CL} , from the reference height, h_0 , nondimensionalized by l_c . Fig. 7 shows that depending on Δ/l_c , different equilibrium configurations can be obtained. Also, it shows that when the contact angle is decreased, the

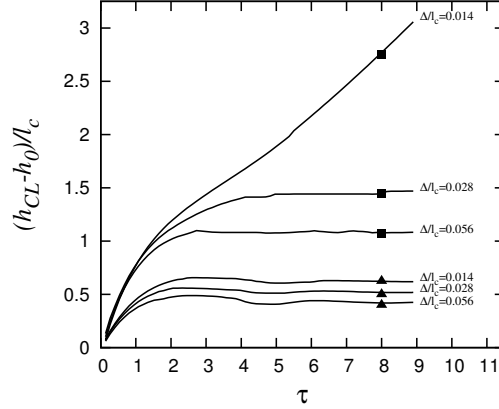


Figure 7: Contact line height as a function of time for $\theta_\Delta = 90^\circ$ (\blacktriangle) and $\theta_\Delta = 60^\circ$ (\blacksquare) at various Δ/l_c . For $\Delta/l_c = 0.014$ and $\theta_\Delta = 60^\circ$, the contact line elevation continues increasing as τ increases. In this figure, $Ca = 0.03$.

contact line is raised to a new equilibrium height for the large grid sizes while a stationary meniscus cannot be achieved for the smallest grid size.

Next, we elaborate on the stationary state results in detail. Figs. 8(a)-(d) show the nondimensional stationary contact line height $(h_\infty - h_0)/l_c$, where $h_\infty = h_{CL}(\tau \rightarrow \infty)$, as a function of the nondimensional mesh size, Δ/l_c , for various capillary numbers and for various contact angles, $90^\circ \leq \theta_\Delta \leq 50^\circ$. The results show the grid sizes, Δ/l_c , where a stationary meniscus forms and no film is deposited on the substrate, for the range of considered θ_Δ .

More importantly, the results show that the computed height of the contact line is a function of Δ/l_c and that for small enough θ_Δ no steady state meniscus can be attained when $\Delta/l_c \leq 0.014$. This lower limit of θ_Δ , for which steady state contact lines can be achieved, gets larger as Ca is increased. The results clearly depend on the chosen value for the smaller mesh size near the contact line, an effect that is expected and will be explained below. This dependence of the results with mesh refinement becomes more marked as Ca is increased or θ_Δ is decreased.

Next we present the results, for which the contact line continues to move upward and a liquid film is then deposited on the substrate. We can understand the onset of film deposition, i.e. the forced dewetting transition, as when the balance between the surface tension and viscous forces close to the contact line region can no longer hold, resulting in wetting failure. (We note that gravity is only involved, asymptotically, in the outermost region.) At the transition, however, we will need to allow the computations to run for a very long time in order to determine when the contact line motion along the wall cannot reach a stationary state. For efficient and accurate determination of the numerical values of the transition Ca_{cr} , we propose a procedure as follows. Fig. 9(a) shows

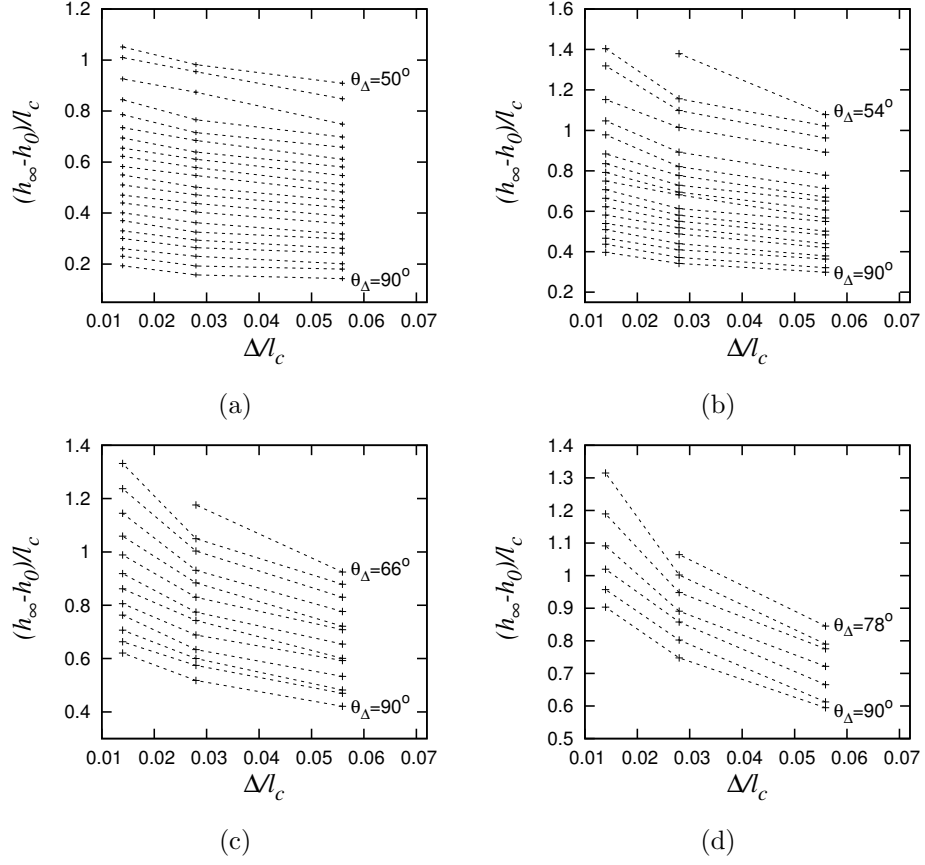


Figure 8: Nondimensional stationary contact line height, $(h_\infty - h_0)/l_c$, as a function of the nondimensional mesh size, Δ/l_c , for (a) $Ca = 0.01$, (b) $Ca = 0.02$, (c) $Ca = 0.03$, and (d) $Ca = 0.04$, for various contact angles, θ_Δ ; the contact angle difference between each set is 2° . For $(Ca, \theta_\Delta) = (0.02, 54^\circ)$, $(0.03, 66^\circ)$, and $(0.04, 78^\circ)$, no steady state menisci can be attained when $\Delta/l_c \le 0.014$.

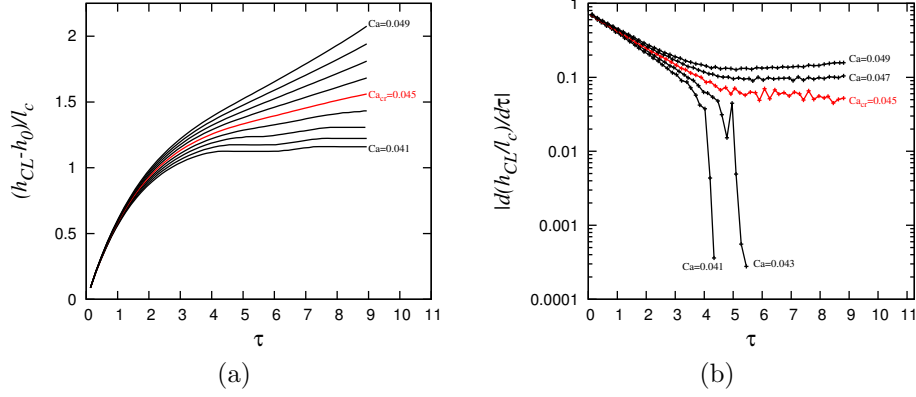


Figure 9: (a) Contact line height as function of time. The increment in Ca is 0.01 and the red line indicates the critical capillary number $Ca_{cr} = 0.045$. (b) Contact line velocity relative to the substrate velocity as a function of time. At the critical capillary number $Ca_{cr} = 0.045$, depicted in red, the transition occurs. $\theta_\Delta = 90^\circ$ and $\Delta/l_c = 0.007$.

contact line heights as a function of time for various values of Ca , when $\theta_\Delta = 90^\circ$ and $\Delta/l_c = 0.007$. As shown, for sufficiently small Ca , a stationary meniscus can be reached while for large Ca , the contact line height keeps increasing. We then use the information in Fig. 9(a) to obtain Fig. 9(b). We then pick the transition capillary number, for which the relative velocity of the contact line, $|d(h_{CL}/l_c)/d\tau|$, does not go to zero as a function τ . This critical capillary number Ca_{cr} is depicted in red in Figs. 9(a) and (b). Using the procedure above, we can therefore determine Ca_{cr} with a very good precision. Figs. 10 (a)-(b) show the contact line height, $(h_{CL} - h_0)/l_c$, as a function of nondimensional time, τ , for two mesh sizes, Δ/l_c , when varying the wall contact angle θ_Δ , for a fixed Ca . As shown, the transition from a stationary meniscus not only depends on θ_Δ , but also on Δ/l_c . As illustrated, the transition occurs at a larger θ_Δ for smaller Δ/l_c . This observation begs a further exploration of how the critical capillary number depends on the contact angle and the grid size. We study these effects in what follows.

To shed more light on the transition mechanism, we analyze the flow, for both when a stationary meniscus forms and when a steady state contact line cannot be attained. Fig. 11(a) provides an example of a stationary meniscus for $Ca = 0.043$, $\theta_\Delta = 90^\circ$, and $\Delta/l_c = 0.014$ (for this set of parameters, $Ca_{cr} = 0.52$). The inset shows the magnified flow field and the pressure distribution. Fig. 11(b) shows a magnified view of the contact line region and the computational mesh. The fine structure of the flow field and the pressure distribution in the contact line region are illustrated. As shown, large gradients of velocity and pressure necessitate a high mesh resolution around the contact line region. As illustrated, the interface is highly curved close to the contact line, leading to an intensified pressure gradient around that region, while the pressure gradient remains weak outside the vicinity of the contact line, leading to gentle bending of the interface

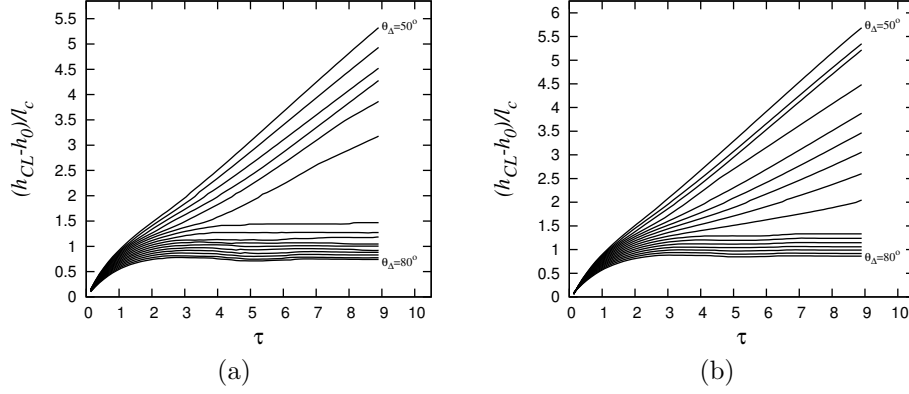


Figure 10: Contact line height as function of time for $50^\circ \leq \theta_\Delta \leq 80^\circ$ and (a) $\Delta/l_c = 0.028$ and (b) $\Delta/l_c = 0.014$; the increment in θ_Δ is 2° . $Ca = 0.03$

away from the contact line.

Fig. 12 shows an example of when the contact line cannot attain a steady state, leading to the formation of a film deposited on the substrate, for $Ca = 0.048$, $\theta_\Delta = 90^\circ$, and $\Delta/l_c = 0.014$ (for this set of parameters, $Ca_{cr} = 0.024$). The figure shows a typical evolution of the interface and the transition to the film. Figs. 12(d)-(f) also show the sagging of the interface behind the contact line after the film formation. The insets of Figs. 12(a)-(c) show the magnified flow field and the pressure distribution. Figs. 12(a)-(c) also show a further magnified view of the contact line region and the flow streamlines. The fine structure of the flow field and the pressure distribution in the contact line region are illustrated. The results reveal the strong pressure gradients close to the contact line region; when capillary forces can no longer balance this strong pressure gradient, the consequence is the wetting failure.

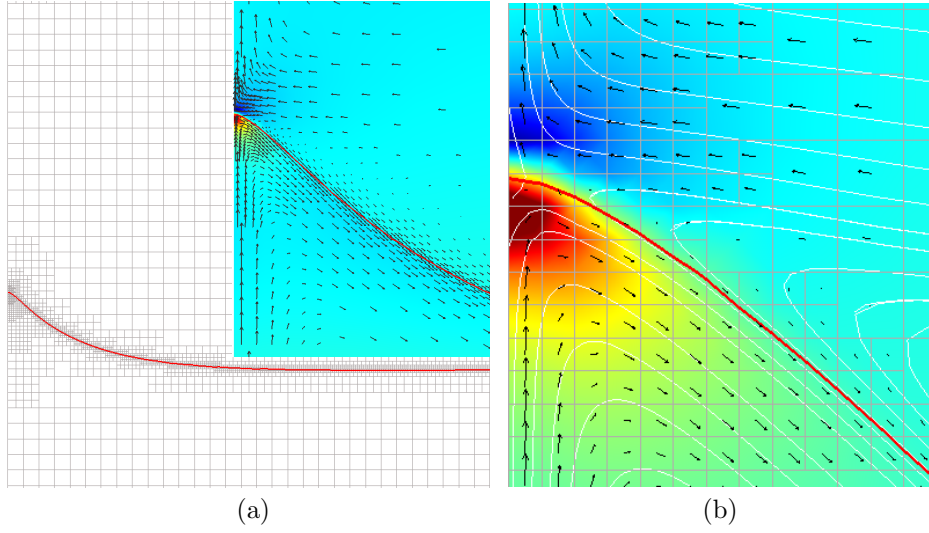
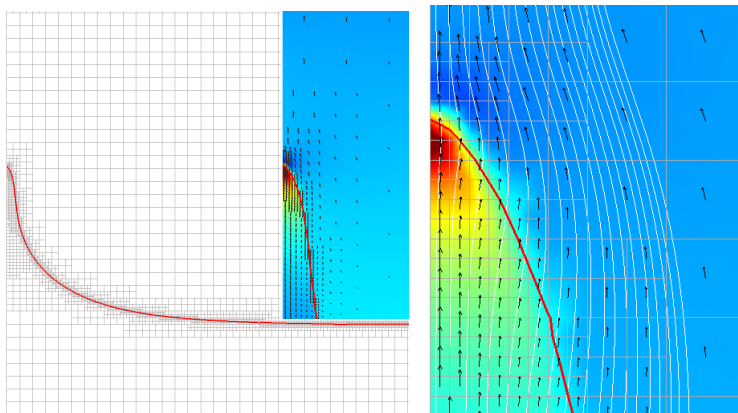
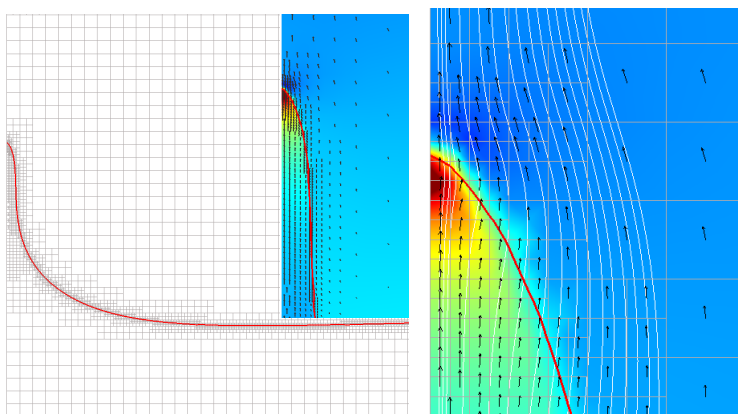


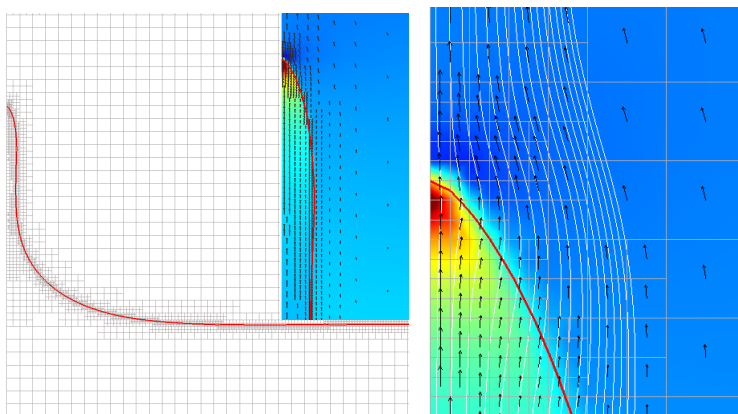
Figure 11: (a) A stationary meniscus forms when $Ca < Ca_{cr}$ as $\tau \rightarrow \infty$. The inset shows the magnified flow field and the pressure distribution. $Ca = 0.043$, $\theta_{\Delta} = 90^\circ$, and $\Delta/l_c = 0.014$. (b) A magnified view of the contact line region and the computational mesh; The fine structure of the flow field and the pressure distribution in the contact line region are illustrated. The pressure colors show the maximum (dark red) and minimum (dark blue) of the pressure distribution.



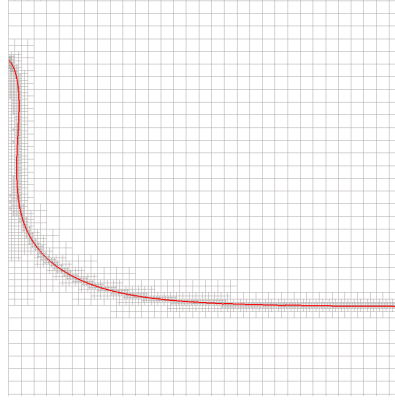
(a)



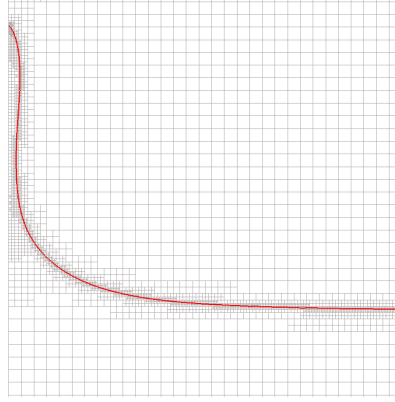
(b)



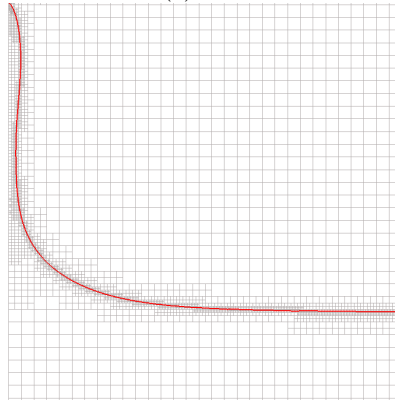
(c)



(d)



(e)



(f)

Figure 12: Time evolution of the interface for $Ca > Ca_{cr}$ at $\tau = 4$ (a), 4.8 (b), 5.9 (c), 6.8 (d), 7.9 (e), 8.7 (f). The insets show the magnified flow field and the pressure distribution. (a)-(c) Right panels show a magnified view of the contact line region and the computational mesh; The fine structure of the flow field and the pressure distribution in the contact line region are illustrated. $Ca = 0.048$, $\theta_{\Delta} = 60^{\circ}$, and $\Delta/l_c = 0.014$. The pressure colors show the maximum (dark red) and minimum (dark blue) of the pressure distribution.

Fig. 13 presents Ca_{cr} as a function of Δ/l_c for a range of θ_Δ for Setups A, B, and C. The symbols are direct simulation results and the solid lines are drawn to guide the eye through a set of points corresponding to the same θ_Δ . In the next section, by systematically investigating the influence of θ_Δ and Δ/l_c on Ca_{cr} , we will develop an improved understanding of the onset of wetting failure. We study the effects of the contact angle and the grid size on Ca_{cr} and give the scaling of it with Δ/l_c .

We also note that our results indicate that the transition coincides with an apparent contact angle $\theta_a = 0$, defining the “apparent contact angle” as the angle at the inflection point, (i.e. where the interface curvature becomes zero). Fig. 14 shows the dependence of the curvature, nondimensionalized by l_c , as a function of the nondimensional vertical distance of the interface from the contact line, $\zeta/l_c = (h_{CL} - y)/l_c$, (see Fig. 1 for the illustration of this vertical distance), for $\theta_\Delta = 60^\circ$ and $\Delta/l_c = 0.014$, at $Ca_{cr} = 0.024$. The results are plotted for $\tau = 6.9$ (here we focus on the time shortly after the film is formed). In Fig. 14, we also plot the angle $\theta(\zeta/l_c)$ that the interface makes with the substrate (red symbols), along with the curvature plot (black symbols), as a function of ζ/l_c . It is clear from these results that $\theta(\zeta/l_c) = 0$ coincides with $\kappa(\zeta/l_c) = 0$, confirming that contact angle is indeed 0 at the transition. Fig. 14 also shows that a significant bending of the interface occurs near the contact line region resulting in a divergent curvature near $\zeta/l_c = 0$.

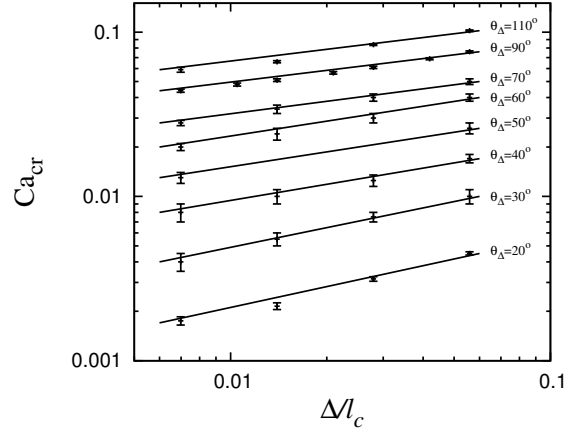
5. Hydrodynamic theories of the dynamic contact line and the dewetting transition

To interpret our numerical results, we will proceed by analogy with the theory of [37, 39]. This theory is valid for small equilibrium contact angles, large viscosity and density ratios and a specific slip length model but we will use the theory of Cox [22] and an analogy to extend it to finite angles and arbitrary viscosity ratios. The problem is analyzed by asymptotic matching of three different regions. 1) A region I near the contact line, where microscopic effects dominate in the physical reality and numerical effects dominate in our simulations. 2) An intermediate region II, where continuum mechanics hold, with surface tension balancing viscous forces, any slip effects are small and gravity effects are negligible. 3) An outer region III, where viscous effects are negligible and surface tension balances gravity.

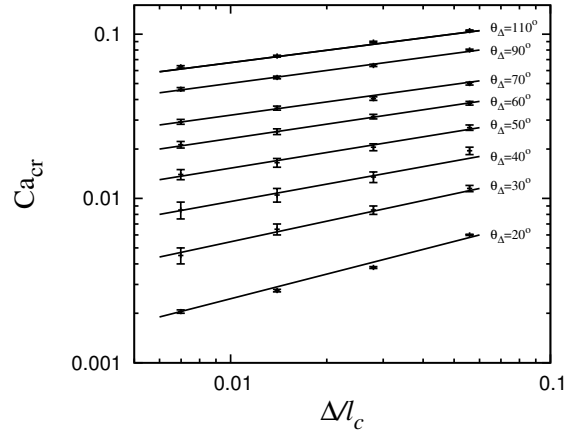
Region II may further be divided into two subregions, a region IIa where the angle is large and a region IIb where the angle is small. The matching between regions IIb and III is performed at a small angle. This is consistent with the remark above that the inflection point is observed at near-zero angle.

The analysis of region I is straightforward, as we make no assumptions about it except that 1) it provides a kind of initial condition for integrating in region II, and 2) as the velocity of the withdrawing plate and the capillary number go to zero, the angle relaxes to the equilibrium angle.

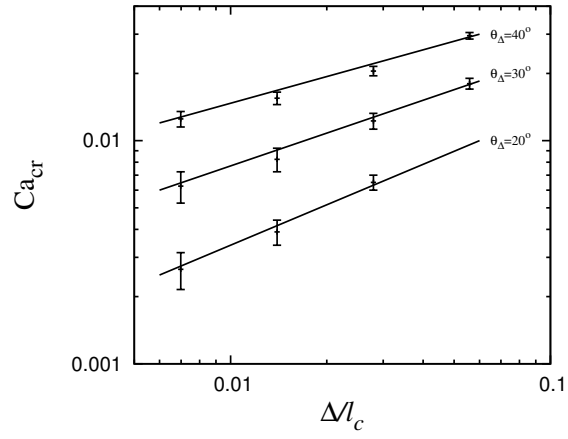
In region II, we assume that the bending, while present, is relatively small so that between two length scales $l_1 < l_2$ the fluid fills approximately a linear



(a)



(b)



(c)

Figure 13: Ca_{cr} as a function of Δ/l_c for a range of θ_Δ for Setups A (a), B (b), and C (c). Symbols present the numerical results and the solid lines are drawn to guide the eye.

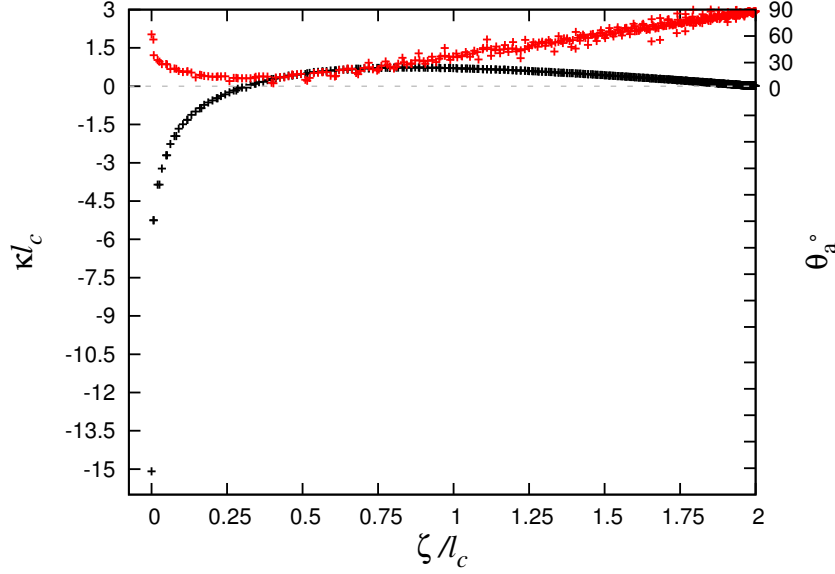


Figure 14: Dependence of the dimensionless curvature (black symbols), nondimensionalized by l_c , and of the angle that the interface makes with the substrate (red symbols), on the nondimensional vertical distance of the interface from the contact line, ζ/l_c , for $\theta_\Delta = 60^\circ$ and $\Delta/l_c = 0.014$, at $Ca_{cr} = 0.024$, plotted for $\tau = 6.9$. Notice that $\theta(\zeta) \simeq 0$, an absolute minimum, at the inflection point, where the curvature also becomes zero.

wedge or dihedron, provided $Ca \ln l_2/l_1$ is small. In that case the fluid that fills the wedge flows according to the wedge solution of Huh & Scriven [19]. This gives a theory for the interface shape as described below. The theory is valid throughout region II, including region IIb, but in region IIb we can also use lubrication theory.

The solution in region III is the famous static meniscus solution [50]. It gives in particular the curvature at the boundary of regions II and III as a function of a contact angle (which is not the microscopic contact angle but an angle that is “apparent” or “seen from region III”) which is undetermined in the static analysis. By letting the contact angle be zero as discussed above one obtains a curvature of $\sqrt{2}/l_c$ [50].

We thus focus on the analysis of region II. In this region, the wedge solution of Huh & Scriven is assumed [19]. It is then possible to use it as done by Cox [22] to obtain the variation of pressure in the wedge and thus by Laplace’s law the variation of curvature. After integration, one may obtain the variation of slope. Cox’s solution in his “intermediate region” identified with our region II, from his Eqs. (7.13) and (7.18) is

$$G[\theta(r)] = G(\theta_e) - Ca \ln(r/\lambda) - Ca \frac{Q_i}{f(\theta_e, q)} + o(Ca), \quad (11)$$

where λ is a characteristic scale for microscopic effects, in our numerical case identified with the grid size through $\Delta \propto \lambda$, θ_e is the equilibrium angle in agreement with our assumption above for the $\text{Ca} \rightarrow 0$ limit, f and G are defined below, and $q = \mu_2/\mu_1$ is the viscosity ratio. Q_i is an integration constant that is obtained by matching with region I and thus depends on region I characteristics. Thus, in our case, Q_i is a function of θ_Δ , but does not depend at first order on the grid size Δ or the capillary number Ca . Since we actually write the first order of an expansion in small Ca , higher-order terms which are small with respect to Ca are also present.

Finally the functions f and G are given by

$$G(\theta) = \int_0^\theta \frac{d\theta'}{f(\theta', q)}, \quad (12)$$

and

$$f(\theta, q) = \frac{2 \sin \theta \{q^2(\theta^2 - \sin^2 \theta) + 2q[\theta(\pi - \theta) + \sin^2 \theta] + [(\pi - \theta)^2 - \sin^2 \theta]\}}{q(\theta^2 - \sin^2 \theta)[(\pi - \theta) + \cos \theta \sin \theta] + [(\pi - \theta)^2 - \sin^2 \theta](\theta - \cos \theta \sin \theta)}.$$

In some specific asymptotic limits, special forms of $G(\theta)$ can be used. For $\theta \ll 1$ and $q = 0$ as in thin liquid film in air situations, it can be shown that

$$G(\theta) \approx \theta^3/9. \quad (13)$$

Also, Sheng and Zhou [51] show that $G(\theta) - G(\theta_e) \approx (\cos \theta_e - \cos \theta)/5.63$ when $q = 1$ and $|\cos \theta| < 0.6$. In this work, we account for $G(\theta)$ using Eq. (12) directly.

Eq. (11) is very attractive because it provides a universal description giving the dependence of $\theta(r)$ on Ca , to the leading order, without any specification of the slip model or any necessity to calculate the details of the macroscopic flow in the outer region. We now match the solution in region II to region III. This is performed using the thin film approximation. It is only an analogy because it requires $q \ll 1$ which is not the case in Setups A and B, but we expect the stress on the thin film boundary to be small even when $q = 1$ because of the disparity of length scales.

In the range $0 < \theta \ll 1$, that is region IIb, we have approximation (13). Moreover, at small angles, $r \sim \zeta = h_{CL} - y$ where we introduced a variable ζ that measures distance away from the contact line along the direction of the solid surface. We also note $\eta(\zeta)$ the local thickness of the film. Then the angle $\theta \sim \eta'(\zeta)$ where we use the notation $\eta' = d\eta/d\zeta$, $\eta'' = d^2\eta/d\zeta^2$, etc.. Thus

$$\eta'(\zeta)^3 \sim 9G(\theta_e) - 9\text{Ca} \ln(\zeta/\lambda) - 9\text{Ca} \frac{Q_i}{f(\theta_e, q)}, \quad (14)$$

where Q_i is determined by the characteristics of the slip region as noticed by Cox. A perhaps more telling notation is to introduce a “microscopic length scale” $r_m = \lambda \exp[f(\theta_e, q)/Q_i]$ in the manner introduced by Voinov [40, 52] so that in the general case

$$G(\theta) = G(\theta_e) - \text{Ca} \ln(r/r_m), \quad (15)$$

while for small angles

$$\theta^3 = \theta_e^3 - 9\text{Ca} \ln(r/r_m). \quad (16)$$

The microscopic length scale r_m encompasses the properties of the microscopic region. Thus the effect of the corresponding small scales can be summarized with two parameters θ_e and r_m . The solution in region IIb, with small angles θ but arbitrary angles θ_e can now be expressed as follows. From Eq. (14), one obtains

$$\eta'(\zeta)^3 \sim 9G(\theta_e) - 9\text{Ca} \ln(\zeta/r_m), \quad (17)$$

which for $\text{Ca} \ll G(\theta_e)$ becomes

$$\eta'(\zeta) \sim [9G(\theta_e)]^{1/3} \left[1 - \frac{\text{Ca}}{G(\theta_e)} \ln(\zeta/r_m) \right]^{1/3}. \quad (18)$$

The above describes the solution at first order in the left part of region IIb. It describes only the left part of that region since the Cox-Voinov approach cannot describe flow between parallel boundaries, for which $\eta' = 0$ and cannot describe regions where $\eta'' > 0$. In other words, the vicinity of the inflection point is not properly described in the Cox-Voinov approach as the “wedge” geometry cannot approximate the flow in that region. The matching between region II and region III must thus be performed by describing the flow through a lubrication equation [53]

$$\eta''' = 3\text{Ca}/\eta^2. \quad (19)$$

Solutions of the lubrication equation (19) will allow us to match the region IIb solution (18) and the outer solution in region III for $\zeta \rightarrow \infty$. In the case of a withdrawing plate, region III is described by the balance between gravity and surface tension, for which a static meniscus solution can be found by quadrature [50]. The approach also applies to other cases, such as a meniscus in a capillary tube where surface tension balances a uniform pressure jump in region III. In both cases, the region III solution is determined up to an unspecified contact angle, which in agreement with the above is set to 0. In that case we have the curvature $\kappa_\infty = \sqrt{2}/l_c$, which becomes upon matching the limiting value at $\zeta \rightarrow \infty$ of the solution of (19). Thus examining the solutions of Eq. (19) provides a connection between the parameters of solution (18) and κ_∞ . The analysis of the Airy function solution of Eq. (19) given in [53] is reproduced in the Appendix. One finds that for ζ small in region II variables,

$$\eta'(\zeta) \sim \{9\text{Ca} \ln[\pi/(2^{2/3}\beta^2\zeta)]\}^{1/3}, \quad (20)$$

where β is a parameter characterizing the Airy function solution of Eq. (19) while for ζ large in region II variables but small in region III variables, that is $\text{Ca}^{-1/3}l_c \ll \zeta \ll l_c$, one has

$$\kappa_\infty \sim (3\text{Ca})^{1/3} \left[\frac{2^{1/6}\beta}{\pi\text{Ai}(s_1)} \right]^2. \quad (21)$$

Eq. (21) is obtained from the Airy function solution, which is parameterized by both β and s_1 . The coefficient β is determined by matching with region II as shown below. The determination of s_1 is more subtle [37, 39]. It is seen that expression (21) predicts a range of possible curvatures depending on the value of s_1 . The smallest possible curvature obtains when the Airy function assumes its global maximum $\text{Ai}(s_{\max}) \simeq 0.53$ for $s_1 = s_{\max} \simeq -1.0$. Thus for a given Ca and β , a critical curvature is given by

$$\kappa_{\infty,cr} = (3\text{Ca})^{1/3} \left[\frac{2^{1/6}\beta}{\pi\text{Ai}(s_{\max})} \right]^2. \quad (22)$$

Indeed if the curvature determined in the outer region III is larger, that is $\kappa_{\infty} > \kappa_{\infty,cr}$, it is always possible to match with a solution parameterized by some s_1 such that $\text{Ai}(s_1) < \text{Ai}(s_{\max})$ and $\text{Ai}(s_{\max})$ small enough. However if curvature $\kappa_{\infty} < \kappa_{\infty,cr}$, the matching is impossible. Thus the critical Ca is given by

$$\kappa_{\infty} = (3\text{Ca}_{cr})^{1/3} \left[\frac{2^{1/6}\beta}{\pi\text{Ai}(s_{\max})} \right]^2, \quad (23)$$

where $\text{Ai}(s_{\max}) \simeq 0.53$ is the global maximum of the Airy function. The parameter β can be determined by comparing Eq. (20) with Eq. (18) which gives

$$\beta^2 \sim \frac{\pi}{2^{2/3}r_m} \exp \left[-\frac{G(\theta_e)}{\text{Ca}} \right], \quad (24)$$

while eliminating β between Eq. (24) and Eq. (23) and using the fact that $\kappa_{\infty} = \sqrt{2}/l_c$ yield

$$\frac{3^{1/3}2^{-5/6}}{\pi\text{Ai}^2(s_{\max})} \frac{\text{Ca}_{cr}^{1/3}l_c}{r_m} \exp \left[-\frac{G(\theta_e)}{\text{Ca}_{cr}} \right] = 1. \quad (25)$$

Our objective in this paper is to apply the above hydrodynamic theory to the study of the numerical model without any special provisions for the contact line dynamics. Thus we identify θ_e to the numerically applied contact angle θ_{Δ} . The microscopic length r_m can be obtained by dimensional analysis. In models that have only a single length scale ℓ , such as slip-length models, or the numerical model, the only dimensionally correct solution is to assume $r_m = \ell/\phi$ where ϕ is a function of the other dimensionless parameters of the model, such as θ_{Δ} and q for the numerical model. It is also dimensionally possible to let ϕ depend on the capillary number Ca , however since Ca is small in the asymptotic approach, one must chose the limit of ϕ for small Ca to be asymptotically consistent. (However an analysis of the numerics that would *not* be asymptotically consistent is also possible but will not be followed in the theoretical analysis below.) Thus in the numerical case where the only length scale is Δ and in the limit $\text{Ca} \ll 1$ and $\Delta \ll l_c$, we represent the microscopic scale r_m as

$$r_m = \Delta/\phi(\theta_{\Delta}), \quad (26)$$

where the “gauge function” ϕ is a non-dimensional measure of the amplitude of the numerical effects on the film near the contact line. In such manner, the expression (26) is connected to the microscopic length scale, $r_m = \lambda \exp[f(\theta_e, q)/Q_i]$, that we introduced earlier, with $\phi(\theta_\Delta) = \exp[-f(\theta_\Delta, q)/Q_i]$. Just as for the function G , we have left the dependence of ϕ on the viscosity ratio q implicit. The gauge function will also appear in the analysis of slip-length models given in Section 6. Thus, by plugging (26) into Eq. (25), one obtains the resulting expression

$$\frac{3^{1/3}2^{-5/6}}{\pi \text{Ai}^2(s_{\max})} \frac{\text{Ca}_{cr}^{1/3} \phi(\theta_\Delta) l_c}{\Delta} \exp \left[-\frac{G(\theta_\Delta)}{\text{Ca}_{cr}} \right] = 1. \quad (27)$$

In our simulations, we measure Ca_{cr} and specify Δ and θ_Δ . This implies that the simulations provide an estimate of the microscopic length gauge $\phi(\theta_\Delta)$

$$\phi(\theta_\Delta) = \frac{\pi \text{Ai}^2(s_{\max})}{3^{1/3}2^{-5/6}} \frac{\Delta}{\text{Ca}_{cr}^{1/3} l_c} \exp \left[\frac{G(\theta_\Delta)}{\text{Ca}_{cr}} \right]. \quad (28)$$

If our theory is valid, it does not only provide a description of the numerics through the gauge function ϕ but it also predicts that the RHS of Eq. (28) is independent of Δ , at least at first order. In Fig. 15, we plot the values of the RHS of (28) for Setups A, B and C. It can be seen that the values of $\phi(\theta_\Delta)$ are concentrated with a small scatter around a nonlinear relationship. This is in favor of our theory since in the RHS of (28) the ratio Δ/l_c varies by an order of magnitude as witnessed by the abscissa in Fig. 13. Moreover the linear behavior of ϕ at small angles is reminiscent of the lubrication theory as we show in the next Section.

6. Comparison with other predictions

It is interesting to compare the above, purely numerical results, to the situation with physical models of the contact line region obtained by other authors. Eggers [54] started with several slip-length models. For the usual Navier slip condition with slip length λ , he obtained the internal solution for interface slope η'

$$\eta'(\zeta) = \theta_e - \frac{3\text{Ca}}{\theta_e^2} \ln \left(\frac{\zeta e \theta_e}{3\lambda} \right), \quad (29)$$

(The expression in Eq. (6) of ref. [37] lacks the factor of 3 in the denominator inside the log term, the correct expression must be deduced from [54].) On the other hand, Eq. (18) becomes, after using the simplified expression (13) for G , valid when $\theta_e \ll 1$,

$$\eta'(\zeta) \sim \theta_e - \frac{3\text{Ca}}{\theta_e^2} \ln \left[\frac{\zeta \phi(\theta_e)}{\lambda} \right]. \quad (30)$$

By comparing Eq. (29) with Eq. (30), we obtain

$$\phi(\theta_e) = e\theta_e/3. \quad (31)$$

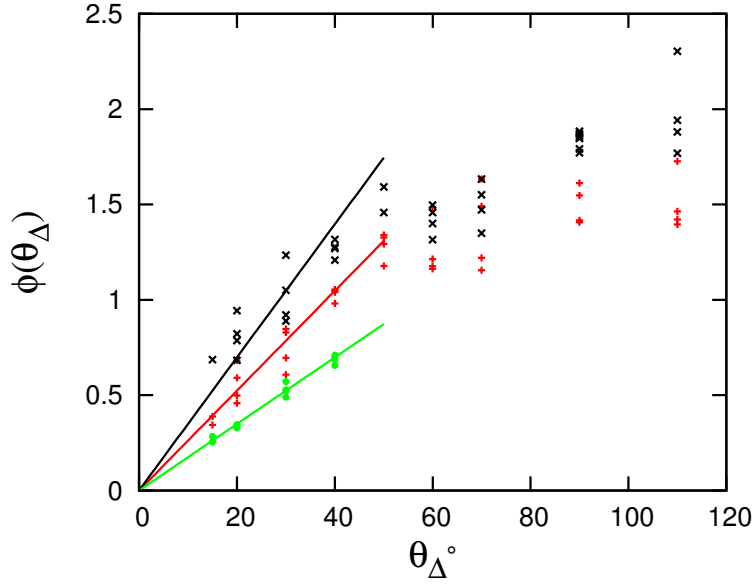


Figure 15: The gauge function ϕ plotted using expression (28) in the text, Setups A (\times), B ($+$), and C (\bullet). Solid lines are $f(x) = 2x$ (\blackline), $f(x) = 1.5x$ (\redline), and $f(x) = x$ (\greenline) (with x measured in radian). For a given angle θ_Δ , the various values of ϕ correspond to the various values of the grid size Δ .

This leads to

$$\kappa_\infty \sim \frac{e}{18^{1/3}\pi\text{Ai}^2(s_{\max})} \frac{\text{Ca}_{cr}^{1/3}\theta_e}{\lambda} \exp\left(-\frac{\theta_e^3}{9\text{Ca}_{cr}}\right), \quad (32)$$

where we have again used expression (13) for G . Expression (32) agrees with the one found in [37, 38, 39] except for a factor of “e” which was not carried over from Eq. (29). An equivalence between the numerical model and the slip length model with $\theta_e = \theta_\Delta$ can be obtained if the numerical length scale $r_m = \Delta/\phi(\theta_\Delta)$ is equalled to the length scale $3\lambda/(e\theta_e)$ appearing in Eq. (30). Then using the small angle approximation $\phi(\theta_\Delta) \simeq a\theta_\Delta$, and $a \approx 1.5$ from Fig. 15 for setup B at $q = 1$, one obtains the equivalent slip length $\lambda = e\Delta/(3a) \simeq 0.6\Delta$. Thus our numerical model may be viewed as having an effective slip of the order of a grid cell. Note that our analysis still holds with $\lambda \simeq 0.9\Delta$ for setup C for $q = 50$ (i.e. $a \approx 1$ from Fig. 15) corresponding to the free-surface setup of asymptotic theory.

7. Dynamic inner contact angle

A possible reinterpretation of Cox’s theory is to consider that the inner region angle is not the equilibrium angle but an angle θ_{in} depending on the contact line velocity so that

$$\theta_{in} = f_\theta(\text{Ca}, q), \quad (33)$$

where dependence on the fluids and solid material properties is implicit. Then Eq. (11) must be rewritten as

$$G[\theta(r)] = G(\theta_{in}) - \text{Ca} \ln(r/\lambda) - \text{Ca} \frac{Q_i}{f(\theta_{in}, q)} + o(\text{Ca}), \quad (34)$$

and we can proceed as before. We note however that there are two possibilities.

1) The microscopic angle is discontinuous, that is there are two angles, the advancing angle θ_a and the receding angle θ_r , so that $\theta_r < \theta_e < \theta_a$ and that for small Ca , $\theta_{in} \sim \theta_a$ for an advancing contact line and $\theta_{in} \sim \theta_r$ for a receding contact line.

2) The microscopic angle is continuous so that at first order

$$\theta_{in} \sim \theta_e + \text{Ca} f'_{\text{Ca}}, \quad (35)$$

with f'_{Ca} a constant. In case of option 2) and small Ca , Eq. (34) can be rewritten at first order in Ca in the form of Eq. (11)

$$G[\theta(r)] = G(\theta_e) - \text{Ca} \ln(r/\lambda) - \text{Ca} \frac{Q'_i}{f(\theta_e, q)} + o(\text{Ca}) \quad (36)$$

the change in microscopic angle with Ca being absorbed into the new integration constant Q'_i . We note that the relation (35) is in agreement with the Molecular

Kinetics Theory (MKT) of Blake and Haynes [55], which states that the contact line is displaced by small random molecular jumps at the surface of the solid due to thermal fluctuations. The average size of these small jumps is determined by the intermolecular interactions between the liquid and solid. The frequency of these random molecular jumps and the average distance of each jump can either be determined empirically or by direct comparison to molecular dynamics simulations. This model postulates that there is an out-of-balance surface tension force, of non-hydrodynamic origin, as a result of the contact line moving on a solid surface. The model then relates the contact line speed to this driving force, resulting in a dynamic contact angle.

The idea of a continuous variation of the inner angle is also the likely outcome of the numerical model, at least when Ca is not too small. We have conducted tests of the numerical model for advancing menisci for Ca down to 10^{-6} , although the dewetting transition itself was studied only for $Ca > 10^{-4}$. For very small Ca , the contact line evolves in an irregular manner, with intermittent spikes in velocity akin to the motion on a rough surface. These spikes have a time periodicity of $T = \Delta/V_s$ as if the interface was pinned with spatial periodicity equal to the grid size Δ . However, no such irregularity is observed for $Ca = 10^{-4}$. Thus we may infer that at least in the range of parameters used in this study, the contact angle is a continuous function of Ca .

8. Outline of a procedure for mesh-independent computations

In the computation of a number of problems involving dynamics contact lines, such as droplet spreading, drop impact or drop sliding on inclined plates, the result typically varies with grid resolution because of hydrodynamic effects. In [26], two of the authors of the present work (S. Afkhami and S. Zaleski) suggested a manner (hereafter called the “AZB” model) of compensating for this hydrodynamic effect, by adjusting the numerical contact angle with the grid resolution. The theory was deemed applicable in the range defined by Sheng and Zhou [51], that is $q = 1$ and $|\cos \theta| < 0.6$. The resulting expression for the variation of the numerical contact angle was

$$\cos(\theta_\Delta) - \cos(\theta_a) = 5.63 Ca \ln \left(\frac{2K}{\Delta} \right), \quad (37)$$

where K is a constant having the dimension of a length, and θ_a is a reference angle that parameterizes, together with K , the “AZB” model. If for a given Ca , K , and θ_a , the grid size and θ_Δ are varied in accordance with expression (37), then the grid dependence of the simulations is reduced. There is no universal choice for K . Instead, the pair K and θ_a needs to be fixed from experimental observations or theoretical models of the contact line, so that θ_a is an approximation of the angle at the length scale K , provided K lies in the region of the validity of Cox’s theory, that is region II in the present work, or the equivalent of region II for a given problem.

From our analysis above, it is clear that the AZB approach defines a length scale K analogous to the microscopic length r_m above and assuming that $K =$

r_m is constant misses the effect of the gauge function ϕ that appears as $r_m = \Delta/\phi(\theta_a)$ and therefore $K/\Delta = 1/\phi(\theta_a)$. Moreover, as stated, the AZB approach is limited to $q = 1$ and $|\cos \theta| < 0.6$. To overcome these limitations, we can use the general approach of Cox and rewrite Eq. (15) as

$$G(\theta) = G(\theta_\Delta) - \text{Ca} \ln \left[\frac{r}{\Delta/\phi(\theta_\Delta)} \right]. \quad (38)$$

If for a given reference angle θ_a and a reference length $K = r_a$ we constrain the numerical angle θ_Δ to vary with grid size such that

$$G(\theta_\Delta) = G(\theta_a) - \text{Ca} \ln \left[\frac{\Delta/\phi(\theta_\Delta)}{r_a} \right], \quad (39)$$

then the theory predicts that simulations should be independent of grid size, provided Δ lies in or “below” region II, and that $\Delta \ll l_{out}$, $\text{Ca} \ll 1$ and $\text{Re} = \mathcal{O}(1)$ where the subscript *out* indicates the outer or region III length scale at which the theory approach is not valid anymore. This can be seen by summing Eq. (38) and Eq. (39) to obtain

$$G(\theta) = G(\theta_a) - \text{Ca} \ln \left(\frac{r}{r_a} \right), \quad (40)$$

valid for r in region II. It is seen that all dependence on the adjustable simulation parameters Δ and θ_Δ is eliminated in the limit of small Ca and small Δ/l_c , realizing the grid independence of converged simulations. Conversely, any prescription for the large scale angle *other* than the form Eq. (39) leads to a dependence of the simulation results on θ_Δ and Δ . It is interesting to discuss the limitations of this approach in terms of Ca and Re .

1) Too large values of Ca lead to a paradox. The model (40), with specified θ_a, r_a , leads to a value of Ca_{cr} given by Eq. (25) with the substitution $\theta_e = \theta_a$ and $r_m = r_a$. If $\text{Ca} > \text{Ca}_{cr}$, then the choice of reference values θ_a, r_a is inconsistent and a different numerical approach including some sort of thin film modeling should be used instead; this is beyond the scope of this paper.

2) Even if $\text{Ca} < \text{Ca}_{cr}$ but Ca is still not very small, values of Δ that are too large or too small compared to r_a lead to $\theta_\Delta < 0$ or $> \pi$, albeit these “critical” values of Δ increase or decrease exponentially as $\exp(\pm 1/\text{Ca})$. Thus there is again a range in which the model can be used. In order to be useful when Ca is not very small, the value of r_a should not be too different from the values of Δ used in practice.

3) The asymptotic limit in which the developments are valid is $\text{Ca} \rightarrow 0$. Perturbations of higher order in the small parameter Ca would create non-convergence effects.

4) Large values of Re are also threatening the validity of the procedure for grid-independent computations. The relations (38) and (39) will be valid if inertial effects can be neglected in the corresponding range of scales, that is $\text{Re}(\Delta) = \rho_1 V_s \Delta / \mu_1 \ll 1$ and $\text{Re}(r_a) = \rho_1 V_s r_a / \mu_1 \ll 1$.

Another interesting configuration is that of very small capillary numbers. In that case, approximate grid independence can be obtained even without the adjustment relation (40) provided the small expected dependence of the predicted angle on the grid size, of order $\epsilon = \text{Ca} \ln \{\Delta / [\phi(\theta_\Delta) r_a]\}$, is smaller than tolerable errors on the angle in the simulation.

Thus for Ca too large, the grid-independent approach is of limited validity while for Ca too small it is not needed. Its range of applicability is at intermediate Ca numbers roughly $\epsilon < \text{Ca} < \text{Ca}_{cr}$ where ϵ is the tolerable error on the angle in the simulation and Ca_{cr} is the critical number for wetting failure. A final limitation we should point out is that the gauge function required in the procedure is known only for the numerical model described in this paper, and would have to be determined in case a different numerical model was used.

All the above leads to a possible prescription on the use of this approach to obtain realistic and converged simulations in practice. Experimental observations usually lead to measurements of contact angles in the range of visible light microscopy, on the order of microns or more. Such length scales are also much smaller than the capillary length l_c or a microchannel diameter and therefore can be considered to lie in region II where Cox's theory is valid. As a result, the experimental measurements can be used to provide the reference lengths, r_a , and angles, θ_a , for a given pair of fluids and a given solid substrate. In order to verify Cox's theory and the validity of our approximations, a second set of measurements at different length scales must be made. Otherwise, the use of the selection of θ_Δ through the above procedure and for Δ in region II, should provide a set of computations at a variety of grid sizes Δ that converges when $\Delta \rightarrow 0$. The reference lengths and angles, θ_a and r_a , can also be obtained by numerical optimization of the simulation results in region III when they are not available through the experimental measurement in region II.

Finally, molecular dynamic simulations are expected to lead to results rather in region I. However, if conducted at large enough length scales, with sufficient computer power, that can overlap in region II, they can also provide the reference lengths and angles, θ_a and r_a , for the direct numerical simulations using the above procedure.

9. Conclusions

We focus on the problem of forced dewetting transition of a partially wetting plate withdrawn from a reservoir using direct numerical simulations. We provide a numerical dataset for critical capillary number, Ca_{cr} , at which the dewetting transition occurs, as a function of the mesh size, Δ , and the numerically-imposed equilibrium contact angle, θ_Δ . Using the asymptotic hydrodynamic theory of the vicinity of the contact line and matching it to the static theory of menisci, we derive an equation for the effect of Δ and θ_Δ on the larger-scale regions of the simulation. The critical capillary number is then predicted by an implicit equation for Ca_{cr} . This equation contains an unknown gauge function ϕ that characterizes the contact line dynamics and is akin to a coefficient that determines the amount of slip. This gauge function is specific to the numerical

model used. Our numerical simulations allow to quantify this “numerical slip” and confirm that it varies linearly with the grid size Δ .

We suggest a manner in which simulations can be made convergent upon grid refinement, despite the singularity at the contact line. This involves adjusting the numerical contact angle as a function of the grid size. This adaptation of the contact angle involves the numerical gauge function ϕ and improves in several ways over the AZB model in [26]. Indeed it is valid for arbitrary angles and viscosity ratios. However the gauge function ϕ is not known, except for the cases treated in this paper: i) for a specific contact angle numerical procedure, or ii) a Navier slip model. Thus the applicability of the grid-independent model may be limited.

The perspectives of this work are a systematic determination of the gauge function ϕ for a range of contact line models used in practice and the verification of the procedure for grid-independent computations in a number of flows. Such grid independent simulation could in turn be used to analyze the results of experiments on contact line dynamics.

Acknowledgements

This research was supported by Electricité de France (EdF), Contract No. 8610-5910129228 (“Advances in Subgrid Models for Subcooled Flow Boiling in Pressurized Water Reactors”) and NSF grant Nos. DMS-1320037 and CBET-1604351. S. A. gratefully acknowledges the support from CNRS for his visit to Institut Jean Le Rond d’Alembert during the preparation of this paper. S. Z. gratefully acknowledges the support from CNRS and MOST (Taiwan) for supporting his visit to NTU during the preparation and writing of this paper.

The authors thank CINES and its team for the grant of computer time and technical assistance on the OCCIGEN supercomputer in the framework of the GENCI allocation x20162b7325. The authors also thank D. Fuster, G. Galliero, C. Josserand, D. Legendre, I. Lunati, A. Malan, and A.-B. Wang for fruitful discussions. S. Z. gratefully acknowledges helpful discussions with Y. Pomeau on contact line modeling.

Appendix A. Analysis of the lubrication equation

We first outline the Airy function solution of Eq. (19) given in [53]. With the transformation $\eta = (3Ca)^{1/3}H$, Eq. 19 becomes

$$H'''(\zeta) = \frac{1}{H^2(\zeta)}. \quad (\text{A.1})$$

This equation can be turned into Airy’s equation for a new variable $z(s)$, that is $z'' = sz$, upon the substitutions

$$H(\zeta) = z^{-2}(s),$$

and

$$\frac{d\zeta}{ds} = -2^{1/3}z^{-2}(s),$$

whose solution is

$$z(s) = \alpha \text{Ai}(s) + \beta \text{Bi}(s), \quad (\text{A.2})$$

which implies

$$H = \frac{1}{[\alpha \text{Ai}(s) + \beta \text{Bi}(s)]^2}, \quad (\text{A.3})$$

where α and β are two arbitrary constants, while $\zeta(s)$ is an antiderivative of $-2^{1/3}z^{-2}(s)$. After integrating explicitly for $\zeta(s)$, Duffy and Wilson [53] conclude that for $\beta > 0$ and any given α , there is a single branch that behaves as desired for the contact line problem, that it grows monotonically from $H = 0$ for $\zeta = 0$ and for $s \rightarrow \infty$ and has $H \rightarrow \infty$ for $s \rightarrow s_1$ and $\zeta \rightarrow \infty$ where s_1 is a root of

$$\alpha \text{Ai}(s_1) + \beta \text{Bi}(s_1) = 0. \quad (\text{A.4})$$

That single branch cannot go to infinity inside $s \in [s_1, \infty)$, which implies that s_1 is the largest among the countably infinite set of roots of (A.4). Thus the solution can be characterized either 1) by the arbitrary pair α, β ($\beta > 0$) or 2) by β ($\beta > 0$) and s_1 chosen arbitrarily with α given by $\alpha = -\beta \text{Bi}(s_1)/\text{Ai}(s_1)$ provided there is no larger root of (A.4). In what follows, we use the second characterization. It can be verified that

$$\zeta = 2^{1/3}\pi \frac{\text{Ai}(s)}{\beta[\alpha \text{Ai}(s) + \beta \text{Bi}(s)]}, \quad (\text{A.5})$$

is an antiderivative of $-2^{1/3}z^{-2}(s)$ and that it satisfies $\zeta = 0$ for $s \rightarrow \infty$. Thus the solution given parametrically by (A.3) and (A.5) starts at $H = 0$ for $\zeta = 0$ and grows monotonically with $H \rightarrow \infty$ for $\zeta \rightarrow \infty$. Expanding the solution for $s \gg 1$, Duffy and Wilson [53] find that

$$H(\zeta) \sim [-3\zeta(\ln \zeta + c)]^{1/3}, \quad (\text{A.6})$$

where $c = \ln[\pi/(2^{2/3}\beta^2)]$. Differentiating, and returning to the original variable η , leads to

$$\eta'(\zeta) \sim \{9\text{Ca} \ln[\pi/(2^{2/3}\beta^2\zeta)]\}^{1/3}. \quad (\text{A.7})$$

For $\zeta \gg 1$, Eq. (A.3) reduces to

$$H(\zeta) = \frac{1}{2} \left[\frac{2^{1/6}\beta}{\pi \text{Ai}(s_1)} \right]^2 \zeta^2 - \frac{2^{2/3}\text{Ai}'(s_1)}{\text{Ai}(s_1)} \zeta + O(1) \quad (\text{A.8})$$

Differentiating twice, one obtains the second derivative. As discussed in Sec. , it is possible to equate the curvature with the second derivative since 1) $\text{Ai}'(s_1) = 0$, and 2) the curvature is of the order of l_c^{-1} and the matching is performed at distances small in the region III variables thus over distances $\zeta \ll l_c$. Over such distances, the curvature of the parabola (A.8) is close to the curvature at its

apex. Reverting to the original variable η , we obtain the curvature $\kappa_\infty \simeq \eta''(\zeta)$ in the asymptotic range $\text{Ca}^{-1/3}l_c \ll \zeta \ll l_c$ as

$$\kappa_\infty \sim (3\text{Ca})^{1/3} \left[\frac{2^{1/6}\beta}{\pi\text{Ai}(s_1)} \right]^2. \quad (\text{A.9})$$

References

- [1] A. A. Darhuber, S. M. Troian, J. M. Davis, S. M. Miller, S. Wagner, Selective dip-coating of chemically micropatterned surfaces, *J. Appl. Phys.* 88 (2000) 5119.
- [2] L. Li, R. J. Braun, K. L. Maki, W. D. Henshaw, P. E. King-Smith, Tear film dynamics with evaporation, wetting, and time-dependent flux boundary condition on an eye-shaped domain, *Phys. Fluids* 26 (2014) 052101.
- [3] H. Kim, J. Buongiorno, Detection of liquid-vapor-solid triple contact line in two-phase heat transfer phenomena using high-speed infrared thermometry, *Int. J. Multiphase Flow* 37 (2011) 166.
- [4] A. Guion, D. Langewisch, J. Buongiorno, Dynamics of the liquid microlayer underneath a vapor bubble growing at a heated wall, *Proceedings of the ASME Summer Heat Transfer Conference* (2013) 14.
- [5] E. H. Kimbrel, A. L. Herring, R. T. Armstrong, I. Lunati, B. K. Bay, D. Wildenschild, Experimental characterization of nonwetting phase trapping and implications for geologic CO₂ sequestration, *Int. J. Greenh. Gas Con.* 42 (2015) 1.
- [6] K. Mahady, S. Afkhami, L. Kondic, A volume of fluid method for simulating fluid/fluid interfaces in contact with solid boundaries, *J. Comp. Phys.* 294 (2015) 243.
- [7] H. Ding, P. D. M. Spelt, Wetting condition in diffuse interface simulations of contact line motion, *Phys. Rev. E* 75 (2007) 046708.
- [8] P. Yue, J. J. Feng, Wall energy relaxation in the Cahn–Hilliard model for moving contact lines, *Phys. Fluids* 23 (2011) 012106.
- [9] P. Seppacher, Moving contact lines in the Cahn–Hilliard theory, *Int. J. Eng. Sci.* 34 (1996) 977.
- [10] L. M. Pismen, Y. Pomeau, Disjoining potential and spreading of thin liquid layers in the diffuse-interface model coupled to hydrodynamics, *Physical Review E* 62 (2) (2000) 2480.
- [11] Y. Pomeau, Contact line moving on a solid, *The European Physical Journal Special Topics* 197 (2011) 15.

- [12] Y. Shikhmurzaev, Moving contact lines in liquid/liquid/solid systems, *J. Fluid Mech.* 334 (1997) 211.
- [13] J. Sprittles, Y. Shikhmurzaev, Finite element simulation of dynamic wetting flows as an interface formation process, *J. Comput. Phys.* 233 (2013) 34.
- [14] L. M. Hocking, A moving fluid interface on a rough surface, *J. Fluid Mech.* 76 (1976) 801.
- [15] T. D. Blake, The physics of moving wetting lines, *J. Colloid Interface Sci.* 299 (2006) 1.
- [16] D. Bonn, J. Eggers, J. Indekeu, J. Meunier, E. Rolley, Wetting and spreading, *Rev. Mod. Phys.* 81 (2009) 739.
- [17] J. H. Snoeijer, B. Andreotti, Moving contact lines: Scales, regimes, and dynamical transitions, *Annu. Rev. Fluid Mech.* 45 (2013) 269.
- [18] Y. Sui, H. Ding, P. D. M. Spelt, Numerical simulations of flows with moving contact lines, *Annu. Rev. Fluid Mech.* 46 (2014) 97.
- [19] C. Huh, L. E. Scriven, Hydrodynamic model of steady movement of a solid/liquid/fluid contact line, *J. Colloid Interface Sci.* 35 (1971) 85.
- [20] H. P. Greenspan, On the motion of a small viscous droplet that wets a surface, *J. Fluid Mech.* 84 (1978) 125.
- [21] E. B. Dussan V., On the spreading of liquids on solid surfaces: Static and dynamic contact lines, *Annu. Rev. Fluid Mech.* 11 (1979) 317.
- [22] R. G. Cox, The dynamics of the spreading of liquids on a solid surface. Part 1. Viscous flow, *Phys. Fluids* 168 (1986) 169.
- [23] M. Renardy, Y. Renardy, J. Li, Numerical simulation of moving contact line problems using a volume-of-fluid method, *J. Comput. Phys.* 171 (2001) 243.
- [24] P. D. Spelt, A level-set approach for simulations of flows with multiple moving contact lines with hysteresis, *J. Comput. Phys.* 207 (2005) 389.
- [25] O. Devauchelle, C. Josserand, S. Zaleski, Forced dewetting on porous media, *J. Fluid Mech.* 574 (2007) 343.
- [26] S. Afkhami, S. Zaleski, M. Bussmann, A mesh-dependent model for applying dynamic contact angles to VOF simulations, *J. Comput. Phys.* 228 (2009) 5370.
- [27] S. Manservigi, R. Scardovelli, A variational approach to the contact angle dynamics of spreading droplets, *Comput. Fluids* 38 (2009) 406.
- [28] P. Joseph, P. Tabeling, Direct measurement of the apparent slip length, *Phys. Rev. E* 71 (2005) 035303.

- [29] E. Lauga, M. Brenner, H. Stone, *Microfluidics: The No-Slip Boundary Condition*, Springer Berlin Heidelberg, 2007, Ch. 15, pp. 1219–1240.
- [30] J. A. Moriarty, L. W. Schwartz, Effective slip in numerical calculations of moving-contact-line problems, *J. Eng. Math.* 26 (1992) 81.
- [31] O. Weinstein, L. M. Pismen, Scale dependence of contact line computations, *Math. Model. Nat. Phenom.* 3 (2008) 98.
- [32] Y. Sui, P. D. M. Spelt, An efficient computational model for macroscale simulations of moving contact lines, *J. Comp. Phys.* 242 (2013) 37.
- [33] D. Legendre, M. Maglio, Comparison between numerical models for the simulation of moving contact lines, *Comput. Fluids* 113 (2015) 2.
- [34] K. Mahady, S. Afkhami, L. Kondic, A numerical approach for the direct computation of flows including fluid-solid interaction: modeling contact angle, film rupture, and dewetting, *Phys. Fluids* 28 (2016) 062002.
- [35] L. D. Landau, B. V. Levich, Dragging of a liquid by a moving plate, *Acta Physicochim. URSS* 17 (1942) 42.
- [36] B. V. Derjaguin, On the thickness of a layer of liquid remaining on the walls of vessels after their emptying, and the theory of the application of photoemulsion after coating on the cine film, *Acta Physicochim. URSS* 20 (1943) 349.
- [37] J. Eggers, Hydrodynamic theory of forced dewetting, *Phys. Rev. Lett.* 93 (2004) 094502.
- [38] J. Eggers, Contact line motion for partially wetting fluids, *Phys. Rev. E* 72 (2005) 061605.
- [39] T. S. Chan, J. H. Snoeijer, J. Eggers, Theory of the forced wetting transition, *Phys. Fluids* 24 (2012) 072104.
- [40] O. Voinov, Hydrodynamics of wetting, *Fluid Dynamics* 11 (1976) 714.
- [41] S. Popinet, The Gerris flow solver, <http://gfs.sourceforge.net/>, 1.3.2 (2012).
- [42] S. Popinet, Gerris: a tree-based adaptive solver for the incompressible Euler equations in complex geometries, *J. Comput. Phys.* 190 (2003) 572.
- [43] S. Popinet, An accurate adaptive solver for surface-tension-driven interfacial flows, *J. Comput. Phys.* 228 (2009) 5838.
- [44] R. Scardovelli, S. Zaleski, Direct numerical simulation of free-surface and interfacial flow, *Annu. Rev. Fluid Mech.* 31 (1999) 567.
- [45] S. Afkhami, M. Bussmann, Height functions for applying contact angles to 2D VOF simulations, *Int. J. Numer. Meth. Fluids* 57 (2008) 453.

- [46] P. Y. Lagr  e, L. Staron, S. Popinet, The granular column collapse as a continuum: validity of a two-dimensional Navier–Stokes model with a $\mu(I)$ -rheology, *J. Fluid Mech.* 686 (2011) 378.
- [47] G. Tryggvason, R. Scardovelli, S. Zaleski, *Direct Numerical Simulations of Gas-Liquid Multiphase Flows*, Cambridge University Press, 2011.
- [48] S. Popinet, Rotation of a straight interface, <http://gerris.dalembert.upmc.fr/gerris/tests/tests/rotate.html>.
- [49] G. Borna, A. Cervone, S. Manservigi, R. Scardovelli, S. Zaleski, On the properties and limitations of the height function method in two-dimensional cartesian geometry, *J. Comp. Phys.* 230 (2011) 851–862.
- [50] L. Landau, E. Lifshitz, *Fluid Mechanics*, Pergamon Press, Oxford, 1987.
- [51] P. Sheng, M. Zhou, Immiscible-fluid displacement: Contact-line dynamics and the velocity-dependent capillary pressure, *Phys. Rev. A* 45 (1992) 5694.
- [52] O. Voinov, Wetting: Inverse dynamic problem and equations for microscopic parameters, *J. Colloid Interface Sci.* 226 (2000) 5.
- [53] B. Duffy, S. Wilson, A third-order differential equation arising in thin-film flows and relevant to tanner’s law, *App. Math. Lett.* 10 (1997) 63.
- [54] J. Eggers, Towards a description of contact line motion at higher capillary numbers, *Phys. Fluids* 16 (2004) 3491.
- [55] T. D. Blake, J. M. Haynes, Kinetics of liquidliquid displacement, *J. Colloid Interface Sci.* 30 (1969) 421.